uniandes

MASTER THESIS

The effect of gas bulk rotation on the morphology of the Lyman α line

Author:
Juan Nicolas Garavito Camargo

Supervisor:
Dr. Jaime E. ForeroRomero

A thesis submitted in fulfilment of the requirements
for the degree of Master in Physcis

in the

Astronomy group
Physics Department

April 2015

UNIVERSIDAD DE LOS ANDES

Abstract

Faculty of Science

Physics Department

Master in Physcis

Effect of the gas bulk rotation on the morphology of the Lyman α line

by Juan Nicolas GARAVITO CAMARGO

We present results of radiative transfer calculations to measure the impact of gas bulk rotation on the morphology of the Lyman α emission line in distant galaxies. We model a galaxy as a sphere with an homogeneous mixture of dust and hydrogen at a constant temperature. These spheres undergo solid-body rotation with maximum velocities in the range $0-300$ km s^{-1}and neutral hydrogen optical depths in the range $\tau_{\mathrm{H}} = 10^5-10^7$. We consider two types of source distributions in the sphere: central and homogeneous. Our main result is that rotation introduces a dependence of the line morphology with viewing angle and rotational velocity. Observations with a line of sight parallel to the rotation axis yield line morphologies similar to the static case. For lines of sight perpendicular to the rotation axis both the intensity at the line center and the line width increase with rotational velocity. Along the same line of sight, the line becomes single peaked at rotational velocities close to half the line width in the static case. Notably, we find that rotation does not induce any spatial anisotropy in the integrated line flux, the escape fraction or the average number of scatterings. This is because Lyman α scattering through a rotating solid-body proceeds identical as in the static case. The only difference is the doppler shift from the different regions in the sphere that move with respect to the observer. This allows us to derive an analytic approximation for the viewing-angle dependence of the emerging spectrum, as a function of rotational velocity.

Acknowledgements

To do . . .

Contents

List of Figures

List of Tables

To my parents: Vilma & Edgar

Chapter 1

Introduction

1.1 *Motivation*

It is astonishing how much we can learn from observing and conteplating the Universe. With the discovery of the planets...

Astronomy is unique in the sense that there is only one Universe to observe. Due to the expanding nature of the Universe and that the speed of light is finite, observations of the farther regions of the Universe are also from the youngest stages of the Universe. This allows to observe the evolution of the Universe during redshift.

There are two techniques to observe the Universe, photometry and spectroscopy. Photometric observations measures the flux astronomical objects in different filters. This allows to dereive quantites such as the luminosity and the temperature. While spectroscopic observations would let study in deep detail the spectra of anstronomical objects, in particular the spectra of galaxies reveals properties such as: the popuation of stars in the galaxy, the redshift, the elements that constitute this objects, the characteristics of the instersetellar medium and many more.

In particular the Lymanα emission line is a usefull tool to detect star forming galaxies at high redshift, specially at $z > 2$ which is when the line is shifted to the optical frame. But as discussed in X the morphology of the line is substantially affected by the gas kinematics & distribution, the interstellar gas (IGM) and by the dust.

Understanding the morphology of the Lyα line is a crusial endeavour to understand deeply the properties of galaxies at high redshift. To this aim computer simulations are extremely usefull, models of this properties can be simulated to creat synthetic profiles that can be compared with the observations.

This is an important era to study this high redshift galaxies. Computer simulations techniques have been imporved and more powerfull facilites are now aveilable. Also a new generation of telescopes are being constructed, this telescopes would have the power to observe more deeply in the sky, and new high redshift galaxies are going to be discovered. This would improved our understanding of the high redshift Universe.

1.2 Historical Remarks

The emission of the Lyman α line in galaxies was first predicted by [1] in their work they suggest that

1.3 The Lyman α line in astronomy

The Lyman α (Here after Lyα) emission line is a consecuence of the transition from the first excited level to the ground level of the electrons in the Hydrogen atom. When the electron undergoes in such transition a photon is emitted with an energy of $13.6eV$ which corresponds to a rest wavelenght of $1215.67\mathring{A}$.

The main sources of the Lyman α emission is star formoing galaxies,

1.3.1 Resonant scattering

Hydrogen is the most abundant element in the Universe furthermore the Lymanα line is a very common line. However the transmission of this Lymanα photons through the Hydrogen clouds it's not trivial. There are two main aspects that heavily influce the morphology of the line.

Imagine that for some reason there is one Hydrogen atom which emits a Lyα photon in the middle of a cloud of Hydrogen atoms which are in the ground state. The Lyα photon will be abosrved and re-emitted from the Hydrogen atoms. This process will end up in a random walk in the space, and the photon can escape the cloud at any point in the surface of it.

In the previous situation all the Hydrogen atoms were in rest, if the atoms present proper motions there would be a doppler shift. If an atom have a velocity v an emit

a Lyα photon in the direction opposite to the movement the Lyα photon would be redshifted by an ammount r

1.3.2 Units, Quantities & Definitions

Through this work we will use some units and quantities that perhaps the reader may not be familiar with. Here we define this quantities.

1.3.3 Optical depth and Column Density

1.3.4 Lyα line profile units

The frequency ν_α of a Lyα photon in rest frame is $2.46 \times 10^{15} Hz$, there are two main units in which the frequency of the Lyα alpha photons may be presented in the literature.

The first is a dimensionless vairable x defined as:

$$x \equiv \frac{(\nu - \nu_\alpha)}{\Delta \nu_D} \tag{1.1}$$

Where ν is the frecuency in the observer frame, ν_D is the broadening of the line due to the termal velocity of the Hydrogen atoms v_{th}. Which can be derived assumming that the Hydrogen gas is in thermal equilibrium and follow a Maxwellian distribution.

$$\frac{m_H v_{th}}{2} = K_B T \tag{1.2}$$

Where m_H is the Hydrogen atom mass, K_B the Boltzmann constant and T the temparature, the expresion for v_{th} is then:

$$v_{th} = \sqrt{\frac{2 K_B T}{m_H}} = 128.5 T^{1/2} \frac{m}{s} \tag{1.3}$$

The Doppler shift due to v_{th} would be:

$$\nu' = (1 - \frac{\vec{v_{th}} \cdot \vec{n}}{c})\nu_\alpha \tag{1.4}$$

Which can be expressed in terms of $\Delta \nu_D$ as:

$$\nu_\alpha - \nu' = \Delta \nu_D = \frac{\vec{v_{th}} \cdot \vec{n}}{c} \tag{1.5}$$

It is also common to express the line profile in terms of the velocity V making use of Eq.1.1:

$$V = x v_{th} = \frac{\nu - \nu_{alpha}}{c} \tag{1.6}$$

1.4 Is the Lyα emission line the most prominent line in the Universe?

There were 25 years since the prediction of the Lyα line to the first observation by \citep{Djorgovski and Thompson},

1. Not so popular, why?, dust, gas kinematics

2. what about high z?

3. Symmetry of the line—morphology

1.5 Analytical Models

In the path of understanding the Lyα line profile, ideal situations have been studied in order to obatin analytical models of the profiles. This models provide the theory that would let develope the modern codes enable to This models are the foundations. In this section the most relevant analytical models are explained in the chronological in whcih they have been developed.

1.6 Simulated models & techniques

In the Universe most of the galaxies have, this charactersitics can not be implemented. There are two main paths in which the simulations have done. The first approach is by implementing the properties of galaxies in the codes, such as: The geometry of the gas, the kinematics of the gas and the dust. Meanwhile some other model a realistic galaxy in the sense of gas geometry and kinematics using hydrodynamics techniques. In this section we briefly descript this two techniques.

1.6.1 Monte-Carlo codes

Monte-Caro techniques are used ...

1.6.2 Hydrodynamic codes

1.6.3 Models

Using Monte-Carlo codes multiple geometries and kinematics has been studied. The outflows of gas in the galaxy due to supernova explotions has been studied by X, the main result is outflows lead to a asymmetric profiles ...

1.7 *This Thesis*

In this thesis we study the effect of rotation, an intrinsic characteristic of galaxies, on the morphology of the Lyman α outcoming profile, to this aim we implement a solid body rotation model in the radiative transfer code `CLARA` [25]. All the codes used for the analysis of this work is reproducible and public available in github.

1.7.1 Summary of the thesis

A lot of progress has been done in modelling the Lyα line using radiative trasnfer codes. Properties of the gas kinematics such as outflows/inflows. Geometries such as slabs, spheres, cavities and the propagation of Lyα photons in a clumpy media. Dust effects XX. In this thesis we study the effect of rotation in the morphology of the Lyα profile.

We model a galaxy as an sphere, with an homogeneous mixture of gas and dust. We took the rotation velocity, the optical depth, the viewing angle as free parameters of the model. We also have two different sources of Lyα photons: A central distribution in the galaxy and an homogeneous distribution.

We quantify the effect of rotation with the following characteristics: Escape fraction of Lyα photons, the width of the Lyα line, the average number of scatterings of the Lyα photons and with the position of the Lyα line maxima.

Our main finding is that rotation do have an important effect on the morphology of the Lyα line. Specially in the width of the line and in the position of the maxima. While the average number of scatterings and the scape fraction remain constant.

The line broadens proportional to the rotation velocity, and the flux in the middle of the line increase

The axys of rotation breaks the symmetry of the system, Althogh observers in different viewing angle with respect to the rotation axys observe the same amount of flux of

the Lyα profile. This result lead us to find an approximate analytic solution to model rotation.

We also (Mark Dijkstra) was

1.7.2   The importance of modelling the effect of gas bulk rotation

Modelling the effect of rotation would play a mayor role in

measures of rotation.

1.7.3   Future work

Chapter 2

The effect of gas bulk rotation on the morpohlgy of the Lyα line

J.N. Garavito-Camargo, J.E Forero-Romero & Mark Dijkstra.

abstract

We present results of radiative transfer calculations to measure the impact of gas bulk rotation on the morphology of the Lyman α emission line in distant galaxies. We model a galaxy as a sphere with an homogeneous mixture of dust and hydrogen at a constant temperature. These spheres undergo solid-body rotation with maximum velocities in the range $0 - 300$ km s^{-1}and neutral hydrogen optical depths in the range $\tau_{\rm H} = 10^5 - 10^7$. We consider two types of source distributions in the sphere: central and homogeneous. Our main result is that rotation introduces a dependence of the line morphology with viewing angle and rotational velocity. Observations with a line of sight parallel to the rotation axis yield line morphologies similar to the static case. For lines of sight perpendicular to the rotation axis both the intensity at the line center and the line width increase with rotational velocity. Along the same line of sight, the line becomes single peaked at rotational velocities close to half the line width in the static case. Notably, we find that rotation does not induce any spatial anisotropy in the integrated line flux, the escape fraction or the average number of scatterings. This is because Lyman scattering through a rotating solid-body proceeds identical as in the static case. The only difference is the doppler shift from the different regions in the sphere that move with respect to the observer. This allows us to derive

an analytic approximation for the viewing-angle dependence of the emerging spectrum, as a function of rotational velocity.

2.1 Introduction

The detection of strong Lyα emission lines has become an essential method in extra-galactic astronomy to find distant star-forming galaxies [1–8]. The galaxies detected using this method receive the name of Lyα emitters (LAEs). A detailed examination of this galaxy population has diverse implications for galaxy formation, reionization and the large scale structure of the Universe. Attempts to fully exploit the physical information included in the Lyα line require an understanding of all the physical factors involved in shaping the line. Due to the resonant nature of this line, these physical factors notably include temperature, density and bulk velocity field of the neutral Hydrogen in the emitting galaxy and its surroundings. A basic understanding of the quantitative behavior of the Lyα line has been reached through analytic studies in the case of a static configurations, such as uniform slabs [9–11] and uniform spheres [12]. Analytic studies of configurations including some kind of bulk flow only include the case of a sphere with a Hubble like expansion flow [13]. A more detailed quantitative description of the Lyα line has been reached through Monte Carlo (MC) simulations [9, 14, 15]. In the last two decades these studies have become popular due to the availability of computing power. Early into the 21st century, the first studies focused on homogeneous and static media [16–18]. Later on, the effects of clumpy media [19] and expanding/contracting shell/spherical geometries started to be studied [12, 20, 21]. For a recent review, we refer the interested reader to Dijkstra [22]. Similar codes have applied these results to semi-analytic models of galaxy formation [23, 24] and results of large hydrodynamic simulations [25–27]. Recently, Monte Carlo codes have also been applied to the results of high resolution hydrodynamic simulations of individual galaxies [28–31]. Meanwhile, recent developments have been focused on the systematic study of clumpy outflows [32] and anisotropic velocity configurations [33]. The recent studies of galaxies in hydrodynamic simulations [28–31] have all shown systematic variations in the Lyα line with the viewing angle. These variations are a complex superposition of anisotropic density configurations (i.e. edge-on vs. face-on view of a galaxy), the inflows observed by gas cooling and the outflows included in the supernova feedback process of the simulation. These bulk flows physically correspond to the circumgalactic

and intergalactic medium (CGM and IGM). These effects are starting to be studied in simplified configurations that vary the density and wind characteristics [33, 34]. However, in all these efforts the effect of rotation, which is an ubiquitous feature in galaxies, has not been systematically studied. The processing of the Lyα photons in a rotating interstellar medium (ISM) must have some kind of impact in the Lyα line morphology. Performing that study is the main goal of this paper. We investigate for the first time the impact of rotation on the morphology of the Lyα line. We focus on a simplified system: a spherical gas cloud with homogeneous density and solid body rotation, to study the line morphology and the escape fraction in the presence of dust. We base our work on two independent Monte Carlo based radiative transfer codes presented in [25] and [32]. This paper is structured as follows: In §2.2 we present the implementation of bulk rotation into the Monte Carlo codes, paying special attention to coordinate definitions. We also present a short review of how the Lyα radiative transfer codes work and list the different physical parameters in the simulated grid of models. In §2.3 we present the results of the simulations, with special detail to quantities that show a clear evolution as a function of the sphere rotational velocity. In §2.4 we discuss the implications of our results. In the last section we present our conclusions. The Appendix presents the derivation of an analytic expression to interpret the main trends observed in the Monte Carlo simulations. In this paper we express a photon's frequency in terms of the dimensionless variable $x \equiv (\nu - \nu_a)/\Delta\nu_D$, where $\nu_\alpha = 2.46 \times 10^{15}$ **Hz** is the Lyα resonance frequency, $\Delta\nu_D \equiv \nu_\alpha \sqrt{2kT/m_p c^2} \equiv \nu_a v_{th}/c$ is the Doppler broadening of the line which depends on the neutral gas temperature T or equivalently the thermal velocity v_{th} of the atoms. We also use the parameter a to define the relative line width as $a = \Delta\nu_\alpha/2\Delta\nu_D$, where $\Delta\nu_\alpha$ is the intrinsic linewidth. For the temperature $T = 10^4$K used in our radiative transfer calculations the thermal velocity is $v_{th} = 12.8\,\text{km s}^{-1}$.

2.2   Models of bulk gas rotation

Describing the kinematics of gas rotation in all generality is a complex task, specially at high redshift where there is still missing a thorough observational account of rotation in galaxies beyond $z > 1.0$. Even at low redshifts there is a great variation in the shape of the rotation curve as observed in HI emission as a function of the distance to the galaxy center. However there are two recurrent features. First, in the central galactic region the

velocity increases proportional to the radius, following a solid rotation be-havior. Second, beyond a certain radius the rotation curve tends to flatten. An ab-initio description of such realistic rotation curves in simulations de-pends on having access to the dynamic evolution of all mass components in the galaxy: stars, gas and dark matter. Such level of realism is extremely complex to achieve, specially if one wants to get a systematic description based on statistics of simulated objects. Following the tradition of studies of Lyα emitting systems, we implement a model with simplified geometry. We assume that the gas is homogeneously distributed in a sphere that rotates as a solid body with constant angular velocity. This simple model will contain only one free parameter: the linear velocity at the sphere's surface, $V_{\max}$.

2.2.1   Detailed Implementation of Rotation

In the Monte Carlo code we define a Cartesian coordinate system to describe the position of each photon. The origin of this system coincides with the center of the sphere and the rotation axis is defined to be z-axis. With this choice, the components of the gas bulk velocity field, $\vec{v} = v_x\hat{i} + v_y\hat{j} + v_z\hat{k}$, can be written as

$$v_x = -\frac{y}{R}V_{\max}, \qquad (2.1)$$

$$v_y = \frac{x}{R}V_{\max}, \qquad (2.2)$$

$$v_z = 0, \qquad (2.3)$$

where R is the radius of the sphere and $V_{\max}$ is the linear velocity at the sphere's surface. The minus/plus sign in the x/y-component of the velocity indicates the direction of rotation. In this case we take the angular velocity in the same direction as the $\hat{k}$ unit vector. With these definitions we can write the norm of the angular velocity as $\omega = V_{\max}/R$. For each photon in the simulation we have its initial position inside the sphere, direction of propagation $\hat{k}_{\rm in}$ and reduced frequency $x_{\rm in}$. The photon's propagation stops once they cross the surface of the sphere. At this point we store the position, the outgoing direction of propagation $\hat{k}_{\rm out}$ and the reduced frequency $x_{\rm out}$. We now define the angle θ by $\cos\theta = \hat{k}_{\rm out} \cdot \hat{k} \equiv \mu$, it is the angle of the outgoing photons with respect to the direction of the angular velocity. We use the variable μ to study the anisotropy induced by rotation. Fig. 2.1 shows the geometry of the problem and the important variables.
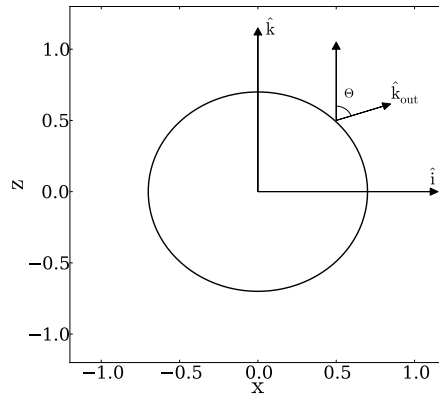
FIGURE 2.1: Geometry of the gas distribution. The angular velocity vector is parallel to the unit vector $\hat{k}$. In order to describe the departures from spherical symmetry we use the polar angle θ formed by the direction of the outgoing photons with respect to the z-axis. We define define the variable $\mu \equiv \cos\theta$ to report to present our results. Computing the spectra for photons in a narrow range of μ is equivalent to having a line-of-sight oriented in that direction.

2.2.2   Brief Description of the Radiative Transfer Codes

Here we briefly describe the relevant characteristics of the two radiative transfer codes we have used. For a detailed description we refer the reader to the original papers [25] and [32]. The codes follow the individual scatterings of Lyα photons as they travel through a 3D distribution of neutral Hydrogen. The frequency of the photon (in the laboratory frame) and its direction of propagation change at every scattering. This change in frequency is due to the peculiar velocities of the Hydrogen absorbing and re-emitting the photon. Once the photons escape the gas distribution we store their direction of propagation and frequency at their last scattering. The initialization process for the Lyα photons specifies its position, frequency and direction of propagation. We select the initial frequency to be exactly the Lyα rest-frame frequency in the gas reference frame and the direction of propagation to be random following an flat probability distribution over the sphere. It means that for photons emitted from the center of the sphere $x_{\rm in} = 0$, while photons emitted at some radii with a peculiar velocity $\vec{v}$ have initial values $x_{\rm in}$ depending on its direction of propagation: $x_{\rm in} = \vec{v} \cdot \hat{k}_{\rm in}/v_{\rm th}$. We do not include the effect of turbulent velocities in the initialization. We neglect this given that the induced perturbation should be on the close to the thermal velocity, $12.8\,{\rm km\ s^{-1}}$, which is one order of magnitude smaller than the velocity widths (100-$500\,{\rm km\ s^{-1}}$) in the static case. If dust is present, the photon can interact either with a Hydrogen atom or dust grain. In the case of a dust interaction the photon can be either absorbed or scattered.
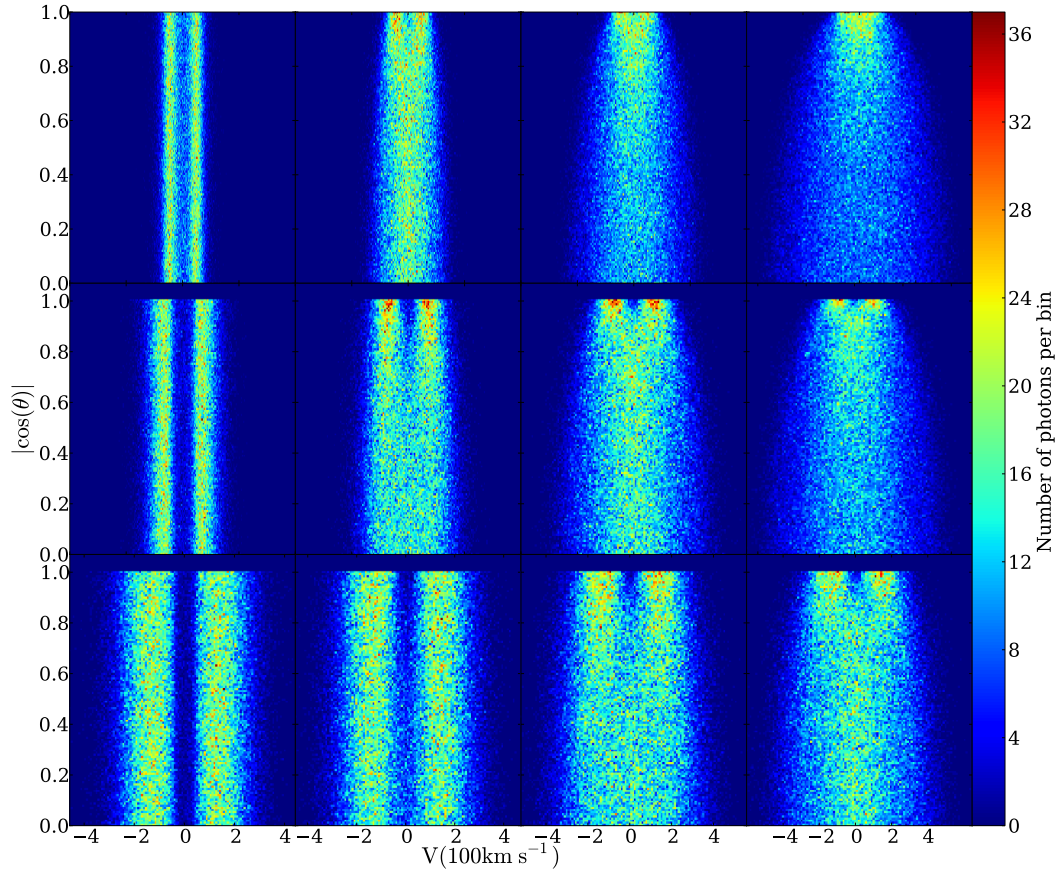
FIGURE 2.2: 2D histogram showing the number of photons that escape with frequency x forming an angle θ (parametrized as $|\cos\theta|$) with the rotation axis. The rotational velocity $(0, 100, 200, 300\,\mathrm{km\,s^{-1}})$ increases from left to right and the optical depth $(10^5, 10^6, 10^7)$ from top to bottom. The Lyα photons are initialized at the center of the sphere. Two main results can be read from this figure. First, the line morphology depends on the viewing angle. Second, the line can become single peaked for high rotational velocities.

This probability is encoded in the dust albedo, A, which we chose to be $1/2$. In order to obtain accurate values for the escape fraction of photons in the presence of dust, we do not use any accelerating mechanism in the radiative transfer. The codes treat the gas as homogeneous in density and temperature. This implies that the gas is completely defined by its geometry (i.e. sphere or slab), temperature T, Hydrogen optical depth τ_{H}, dust optical depth τ_{a} and the bulk velocity field $\vec{v}$.

2.2.3   Grid of Simulated Galaxies

In the Monte Carlo calculations we follow the propagation of $N_\gamma = 10^5$ numerical photons through different spherical galaxies. For each galaxy we
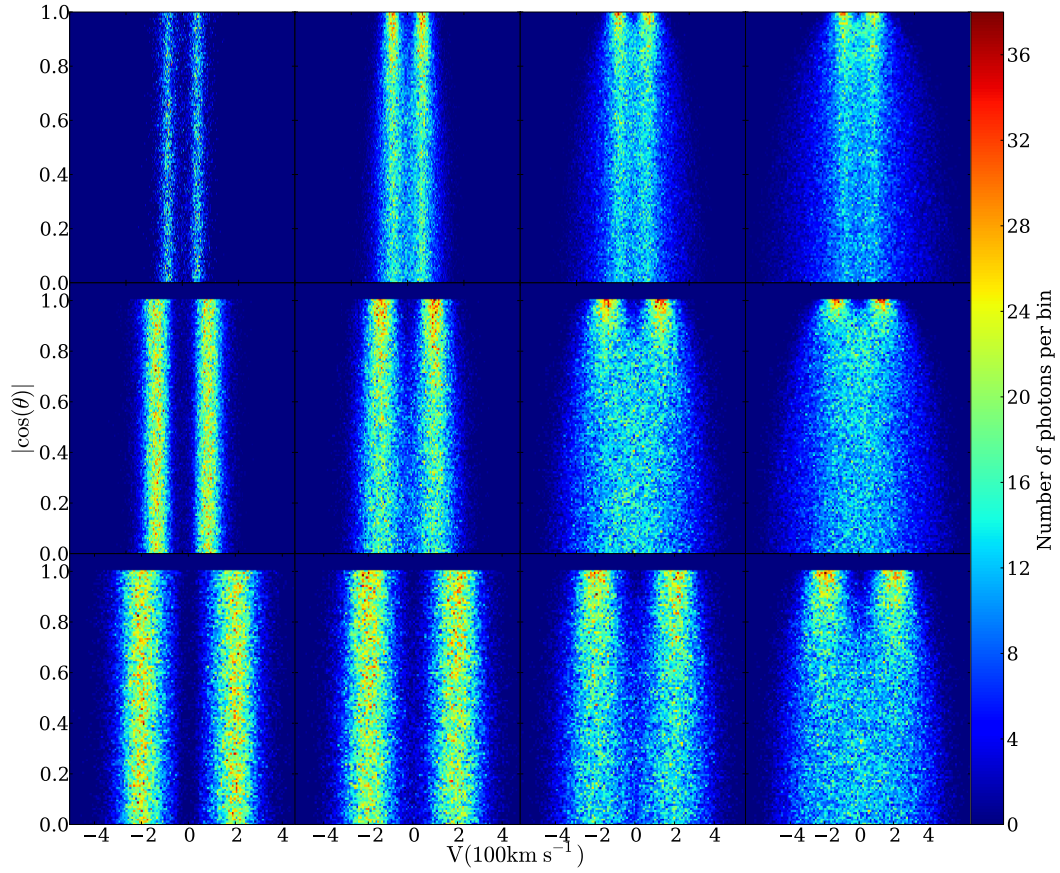
FIGURE 2.3: Same as Fig. 2.2 for Lyα photons initialized homogeneously throughout the sphere.

Physical Parameter (units)	Symbol	Values
Velocity (km s^{-1})	$V_{\max}$	0, 100, 200, 300
Hydrogen Optical Depth	τ_H	10^5, 10^6, 10^7
Dust Optical Depth	τ_a	0,1
Photons Distributions		Central, Homogeneous

TABLE 2.1: Summary of Physical Parameters of our Monte Carlo Simulations.

vary at least one of the following parameters: the maximum rotational velocity $V_{\max}$, the hydrogen optical depth τ_H, the dust optical depth τ_a and the initial distribution of photons with respect to the gas. In total there are 48 different models combining all the possible different variations in the input parameters. Table 2.1 lists the different parameters we used to generate the models. The results and trends we report are observed in both Monte Carlo codes.
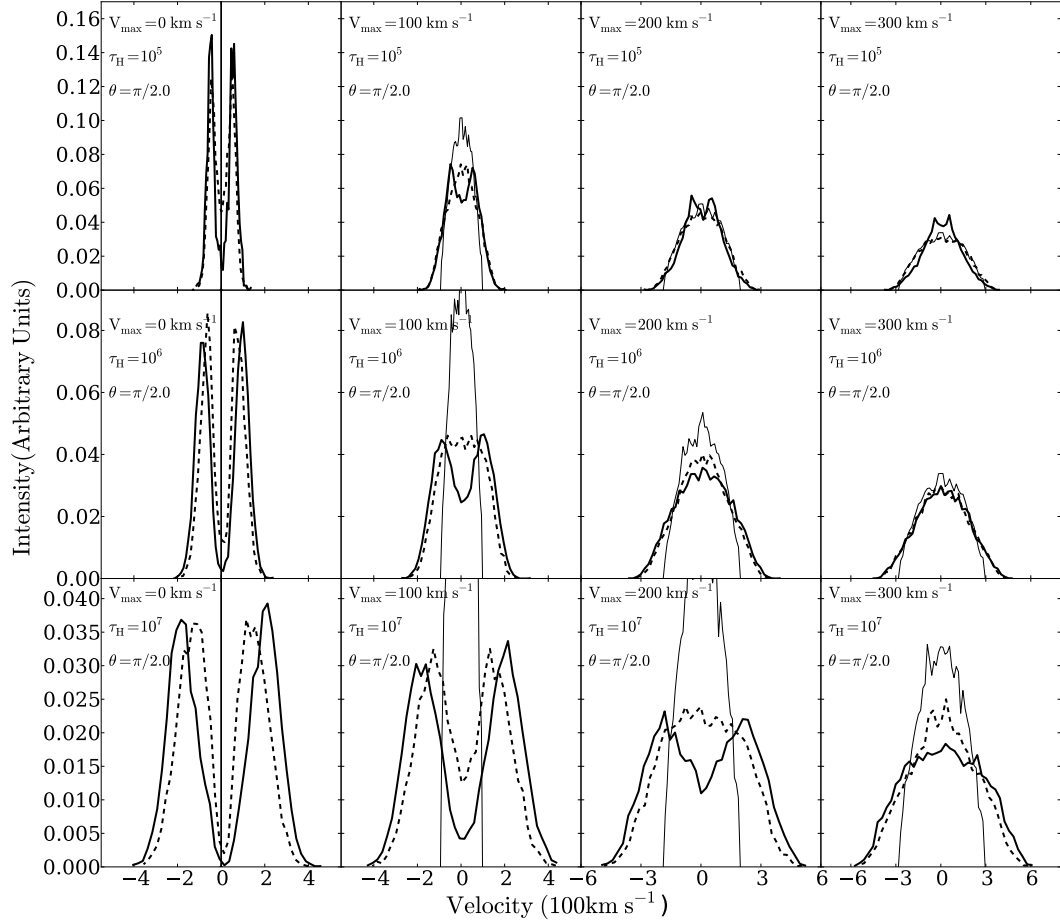
FIGURE 2.4: Shape of the Lyα line for different maximum rotational velocities for a LoS perpendicular to the rotation axis ($|\mu| \sim 0$). The continuous (dashed) line represents the central (homogeneous) source distributions. The continuous thin line represents the intrinsic homogeneous spectrum. The panels follow the same distribution as in Fig.s 2.2 and 2.3.

2.3   Results

The main results of this paper are summarized in Fig. 2.2 and 2.3. They show 2D histograms of the escape frequency x and outgoing angle θ parametrized by $|\mu|$. Taking into account only photons photons around a value of $|\mu|$ gives us the emission detected by an observer located at an angle θ with respect to the rotation axis. We have verified that the solutions are indeed symmetric with respect to $\mu = 0$. We have also verified that the total flux is the same for all μ. From these figures we can see that the line properties change with rotational velocity and depend on the viewing angle θ. In the next subsections we quantify the morphology changes with with velocity, optical depth and viewing angle. We characterize the line morphology by its total intensity, the full width at half maximum, (FWHM) and the location of the
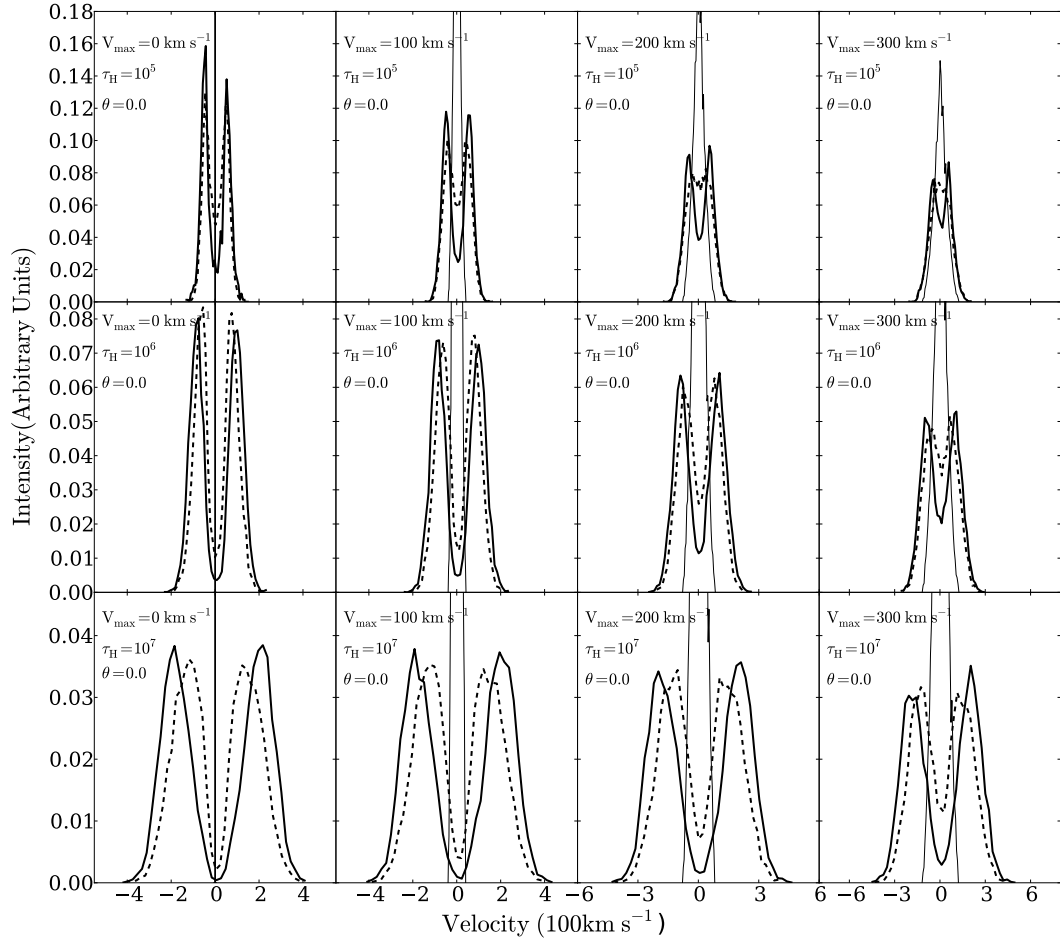
FIGURE 2.5: Shape of the Lyα line for different maximum rotational velocities for a LoS perpendicular to the rotation axis ($|\mu| \sim 1$). The continuous (dashed) line represents the central (homogeneous) source distributions. The continuous thin line represent the intrinsic homogeneous spectrum. The panels follow the same distribution as in Fig.s 2.2 and 2.3.

peak maxima. In order to interpret the morphological changes in the line we also report the median number of scatter for each Lyα photon in the simulation. For the models where dust is included we measure the escape fraction as a function of rotational velocity and viewing angle.

2.3.1 Line Morphology

The first column in both Fig. 2.2 and 2.3 shows that for the static sphere the line properties are independent of $|\mu|$, as it is expected due to the spherical symmetry. However, for increasing rotational velocities, at a fixed optical depth, there are clear signs that this symmetry is broken. If the viewing angle is aligned with the rotation axis, $|\mu| \sim 1$, the Lyα line keeps a double peak with minor changes in the morphology as the rotational velocity increases.
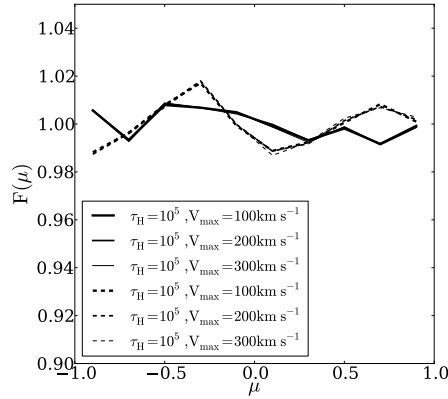
FIGURE 2.6: Integrated flux distribution as a function of the viewing angle as parametrized by μ. Continuous (dashed) correspond to central (homogeneous) source distribution. The models correspond to an optical depth of $\tau_{\mathrm{H}} = 10^5$ and rotational velocities of $100\,\mathrm{km\,s^{-1}}$, $200\,\mathrm{km\,s^{-1}}$ and $300\,\mathrm{km\,s^{-1}}$. The distributions are flat in the range of models probed in this paper, meaning that the integrated flux for all viewing angles is the same.

However, for a line of sight perpendicular to the rotation axis, $|\mu| \sim 0$, the impact of rotation is larger. The double peak readily transforms into a single peak. This is clear in Fig. 2.4 and in Fig. 2.5 where we present the different line morphologies for $|\mu| \sim 0$ and $|\mu| \sim 1$ for the homogeneous and central configurations. The panels have the same distribution as Fig. 2.2 and 2.3. There are three clear effects on the line morphology as the rotational velocity increases. First, the line broadens; second, the double peaks reduce their intensity; and third, the intensity at the line centre rises. The last two effects are combined to give the impression that the double peaks are merged into a single one at high rotational velocities.

2.3.2 Integrated Line Intensity

We now consider possible variations in the integrated flux with respect to the viewing angle θ. To this end we define the normalized flux seen by an observer at an angle μ by:

$$F(\mu) = \frac{2\Delta N}{N\Delta\mu}, \tag{2.4}$$

where $\mu = \cos\theta$, N is the total number of outgoing photons, ΔN is the number of photons in an angular bin $\Delta\theta$. This definition satisfies the condition $\int_{-1}^{1} F(\mu)d\mu/2 = 1$. In the case of perfect spherical symmetry one expects a flat distribution with $F(\mu) = 1$. Fig. 2.6 shows the results for a selection of models with $\tau_{\mathrm{H}} = 10^5$, different rotational velocities and the two types of source distributions. This shows that $F(\mu)$ is consistent with being flat, apart
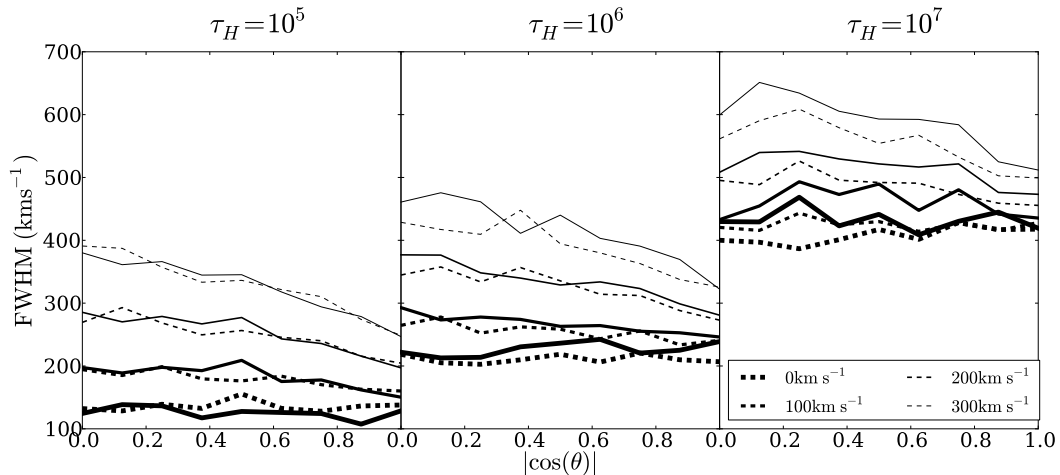
FIGURE 2.7: FWHM for the non-dusty models as a function of the viewing angle parametrized by $|\cos\theta|$. Continuous (dashed) lines correspond to central (homogeneous) source distributions. The general trend is of an decreasing line width as the line of sight becomes parallel to the rotation axis.

from some statistical fluctuations on the order of 2%. This is a remarkable result: while the rotation axis defines preferential direction, the integrated flux is the same for all viewing angles in the range of parameters explored in this paper. This can be understood from the fact that *radiative transfer inside a sphere that undergoes solid-body rotation proceeds identical as inside a static sphere*: we can draw a line between any two atoms within the rotating cloud, and their relative velocity along this line is zero (apart from the relative velocity as a result of random thermal motion), irrespective of the rotation velocity of the cloud. This relative velocity is what is relevant for the radiative transfer[1]

2.3.3 Full Width at Half Maximum

We use the full width at half maximum (FWHM) to quantify the line broadening. We measure this width from the line intensity histogram by finding the values of the velocities at half maximum intensity. We use lineal interpolation between histogram points to get a value more precise than the bin size used to construct the histogram. Fig. 2.7 shows the FWHM for all models as a function of the viewing angle. The FWHM increases for decreasing values of μ (movement from the poles to the equator) and increasing values of $V_{\max}$.

---

[1]This point can be further illustrated by considering the path of individual photons: let a photon be emitted at line center ($x = 0$), in some random direction **k**, propagate a distance that corresponds to $\tau_0 = 1$, scatter fully coherently (i.e. $x = 0$ after scattering in the gas frame) by 90°, and again propagate a distance that corresponds to $\tau_0 = 1$. The position where the photon scatters next does *not* depend on the rotation of the cloud, nor on **k**.
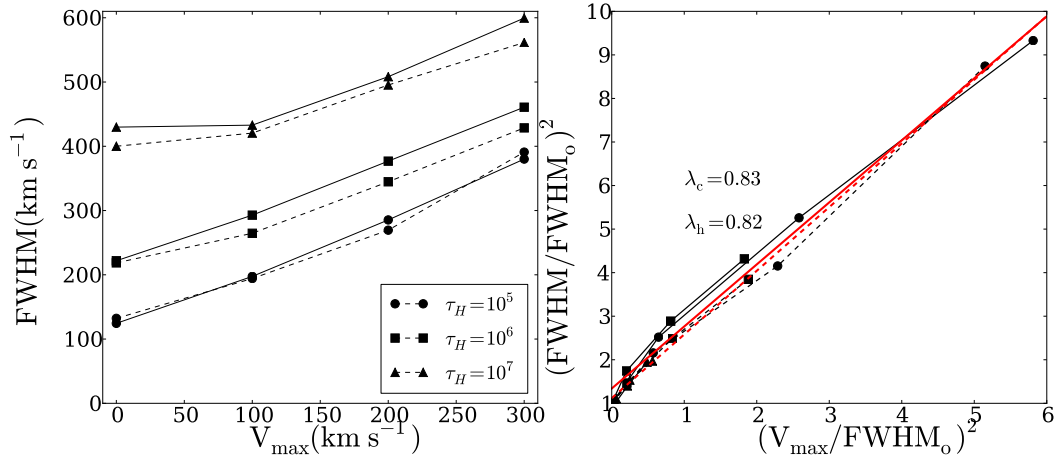
FIGURE 2.8: FWHM for the non-dusty models as a function of rotational velocity $V_{\max}$ for observers located perpendicular to the rotation axis. The left panel shows the results in velocity units while the right panel normalizes the data by the FWHM in the static case. Continuous (dashed) lines correspond to central (homogeneous) source distributions. The straight lines represent the fit to the data using the expression in Eq. (2.5).

In Fig. 2.8 we fix $|\mu| < 0.1$, i.e. viewing angle perpendicular to the rotation axis, to plot the FWHM as a function of rotational velocity. We parametrize the dependency of the line width with $V_{\max}$ as

$$\mathrm{FWHM}^2 = \mathrm{FWHM}_0^2 + V_{\max}^2/\lambda^2, \qquad (2.5)$$

where FWHM_0 is the velocity width in the static case and λ is a positive scalar to be determined as a fit to the data. With this test we want to know to what extent the new velocity width can be expressed as a quadratic sum of the two relevant velocities in the problem. All the models fall into a single family of lines in the plane shown in the right panel of Fig. 2.8, justifying the choice of our parametrization. We fit simultaneously all the points in two separate groups, central and homogeneous sources. We find that these values are $\lambda_{\mathrm{c}} = 0.83 \pm 0.06$ and $\lambda_{\mathrm{h}} = 0.82 \pm 0.05$ respectively.

2.3.4 Line Maxima

We measure the peak maxima position, x_m, to quantify the transition from double into single peak profiles. In Fig. 2.9 we show the dependence of x_m with the viewing angle parametrized by $|\cos\theta|$ for different rotational velocities. There are two interesting features that deserve attention. First, for a viewing angle parallel to the rotational axis ($\mu \sim 1.0$) the maxima of
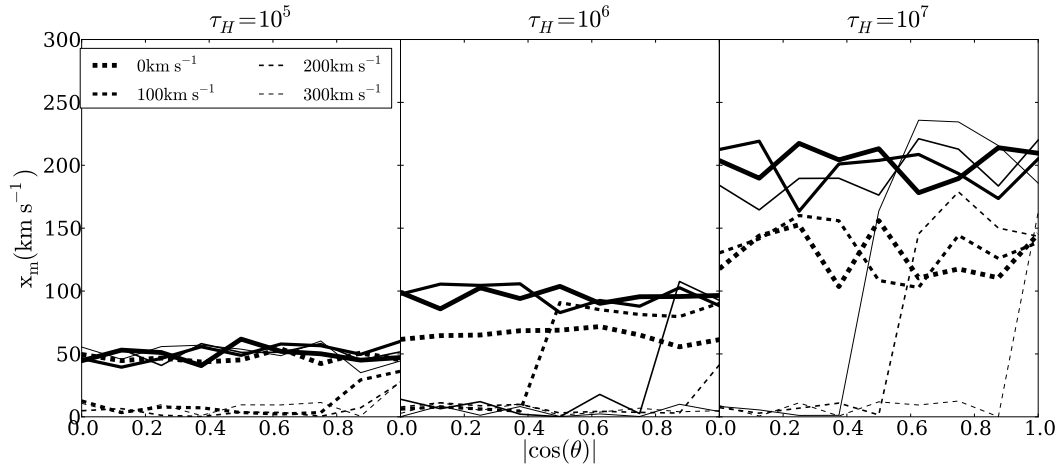
FIGURE 2.9: Position of the line maxima as a function of maximum rotational velocity $V_{\max}$. Continuous (dashed) lines correspond to central (homogeneous) source distributions. A value of $x_{\max} = 0$ indicates that line becomes single peaked.

Source Distribution	τ_H	$V_{\max}$ (km s^{-1})			
		0	100	200	300
Homogeneous	10^5	0.263	0.263	0.263	0.263
	10^6	0.291	0.292	0.293	0.293
	10^7	0.228	0.228	0.228	0.228
Central	10^5	0.096	0.096	0.096	0.096
	10^6	0.066	0.066	0.066	0.066
	10^7	0.015	0.016	0.016	0.015

TABLE 2.2: Escape fraction values for all dusty models.

all models with the same kind of source initialization are similar regardless of the rotational velocity. Second, at a viewing angle perpendicular to the rotation axis ($\mu \sim 0.0$) a large fraction of models become single peaked. This feature appears more frequently for homogeneously distributed sources if all the other parameters are equal.

2.3.5 Dusty Clouds: Escape Fraction

We now estimate the escape fraction f_{esc} for the dusty models. The main result is that we do not find any significant dependence with either the viewing angle nor the rotational velocity. This is consistent with our finding in § **2.3.2**, that radiative transfer inside the cloud does not depend on its rotational velocity. For completeness we list in Table **2.2** the escape fraction for all models. We now put these results in the context of the analytic solution

for the infinite slab[11]. In Neufeld's set-up the analytic solution depends uniquely on the product $(a\tau_H)^{1/3}\tau_A$ where $\tau_A = (1-A)\tau_a$, valid only in the limit $a\tau_H \gg 1$. At fixed values of τ_a the escape fraction monotonically decreases with increasing values of τ_H. This expectation holds for the central sources. But in the case of homogeneous sources the escape fraction increases slightly from $\tau_H = 10^5$ to $\tau_H = 10^6$ The naive interpretation of the analytic solution does not seem to hold for photons emitted far from the sphere's center. We suggest that increasing τ_H from 10^5 to 10^6 causes a transition from the 'optically thick' to the 'extremely optically thick' regime for a noticeable fraction of the photons in the homogeneous source distribution. In the optically thick regime, Lyα photons can escape in 'single flight' which corresponds to a scenario in which the photon resonantly scatters $10^4 - 10^5$ times until it is scattered into the wing of the line ($x \sim 3-4$). At these frequencies the medium is optically thin, and the photons can escape efficiently in a single flight. In contrast, in an extremely optically thick medium Lyα photons escape in a 'single excursion' [9]. Here, photons that are scattered into the wing of the line escape from the medium in a sequence of wing scattering events. In both cases, Lyα photons resonantly scatter 10^4-10^5 times. Because we keep our clouds the same size, the mean free path of Lya photons that scatter resonantly is 10 times larger for the case $\tau_H = 10^5$ than for $\tau_H = 10^6$. If we compute the average distance D travelled by Lyα photons through a medium of size R as a function of line center optical depth τ_H, then we find that during the transition from optically thick to extremely optically thick the mean traversed distance D actually decreases slightly. This decrease is unique to this transition region, and D generally increases with τ_H at other values of τ_H.

2.3.6 Average Number of Scatterings

The number of scatterings affects the escape frequency of a Lyα photon. Studying this quantity further illustrates the independence of the integrated flux and the escape fraction on rotational velocity. In Fig. 2.10 we show the average number of scatterings $\langle N_{\text{scatt}} \rangle$ as a function of the cosinus of the outgoing angle $|\cos\theta|$ and the rotational velocity V_{max}. From the right panel observe that the number of scatterings and the outgoing angle are independent. This plot corresponds to the specific case of the central model with $\tau = 10^5$ and $V_{\text{max}} = 300\,\text{km s}^{-1}$, but we have verified that this holds for all models. The right panel of Fig. 2.10 shows how the average number
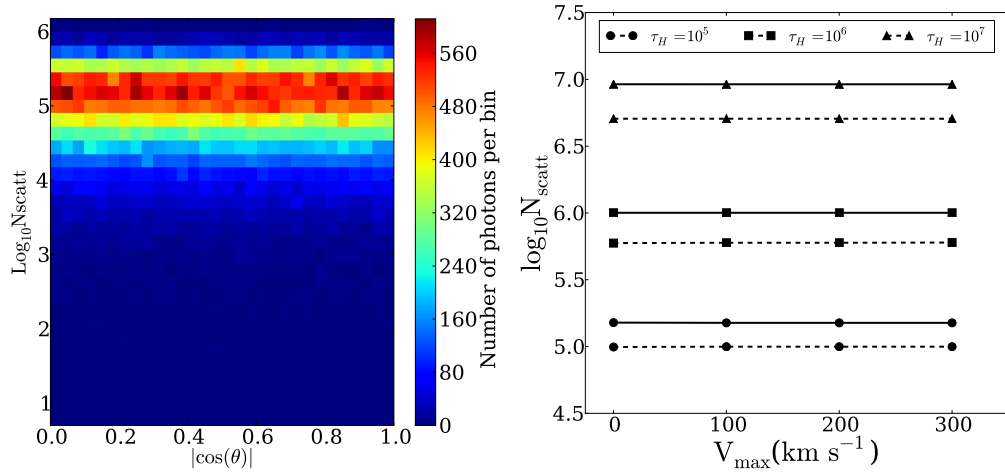
FIGURE 2.10: 2D histogram of the logarithm of the average number of scatterings as function of μ (left) and the maximum rotational velocity $V_{\max}$ (right). The left panel shows the behaviour for $\tau = 10^5$ and $V_{max} = 300\,\mathrm{km\,s^{-1}}$ as a function of $|\cos\theta|$, the color indicates the number of photons per bin. In the right panel the continous (dashed) lines represent the results for the central (homogeneous) model. The independence of N_{scatt} with μ and $V_{\max}$ is present in all models.

of scatterings is also independent from the rotational velocity. The lower number of average scatterings in the homogeneous source distribution is due to a purely geometrical effect. Photons emitted close to the surface go through less scatterings before escaping. In static configurations it is expected that the optical depth correlates number of scatterings. This has been precisely quantified in the case of static infinite slab. In that model for centrally emitted sources the average number of scatterings depends only on the optical depth $\langle N_{\mathrm{scatt}}\rangle = 1.612\tau_{\mathrm{H}}$ [**9**, **10**], for homogeneously distributed sources $\langle N_{\mathrm{scatt}}\rangle = 1.16\tau_{\mathrm{H}}$ [**10**]. In our case we find that for the central model the number of scatterings is proportional to the optical depth, with $\langle N_{\mathrm{scatt}}\rangle = (1.50, 1.00, 0.92)\tau_{\mathrm{H}}$ for optical depth values of $\tau_{\mathrm{H}} = (10^5, 10^6, 10^7)$ respectively. For the homogeneous sources we find that $\langle N_{\mathrm{scatt}}\rangle = (0.99, 0.59, 0.51)\tau_{\mathrm{H}}$.

2.4 Discussion

2.4.1 Towards an analytical description

There is a key result of our simulations that allows us to build an analytical description for the outgoing spectra. It is the independence of the following three quantities with the rotational velocity and the viewing angle: integrated flux, average number of scatterings and escape fraction. As we

explained in § **2.3.2**, the best way to understand this is that radiative transfer inside a sphere that undergoes solid-body rotation proceeds identical to that inside a non-rotating sphere. While scattering events off atoms within the rotating cloud impart Doppler boosts on the Lyα photon, these Doppler boost are only there in the lab-frame. Therefore, in the frame of the rotating gas cloud all atoms are stationary with respect to each other and the scattering process proceeds identical as in the static case (also see § **2.3.2** for an additional more quantitative explanation). This result allows us to analytically estimate the spectrum emerging from a rotating cloud: The spectrum of Lyman α photons emerging from a rotating gas cloud is identical as for the static case in a frame that is co-rotating with the cloud. However, the surface of cloud now moves in the lab-frame. Each surface-element on the rotating cloud now has a bulk velocity with respect to a distant observer. In order to compute the spectrum one can integrate over all the surface elements in the sphere with their corresponding shift in velocity and an additional weight by the surface intensity. Fig **2.11** shows some examples of analytic versus full MC spectra using this approach (the implementation details are in the Appendix). The left panel shows the results for different rotational velocities in the case of $\tau_H = 10^7$ and an observer located perpendicular to the axis of rotation ($i = 0$ in the scheme of Fig **A.1** in the Appendix). The right panel shows the results for different viewing angles in the case of $\tau_H = 10^7$ and a rotational velocity of $V_{\max} = 300\,\mathrm{km\,s^{-1}}$. The two methods clearly give good agreement, though not perfect. In particular, the left panel shows that the MC gives rise to a spectrum that is slightly more concentrated towards the line centre. As we explain in Appendix **A**, we do not expect perfect agreement, because this requires an analytic solution for the spectrum of Lyα photons emerging from a static, optically extremely thick cloud *as a function of the angle at which they escape from the sphere*. This solution does not exist in the literature. It is possible to get better agreement my modifying the surface brightness profile. In any case, the analytic calculation closely captures the results obtained from the full calculations from the MC simulations. As such, they are extremely useful and provide us with a quick tool to verify our calculations at the first order level.

2.4.2 Impact on the interpretation of simulated and observational data

We now compare our findings to other computational results and discuss its possible implications for the interpretation of observational data. Escape at
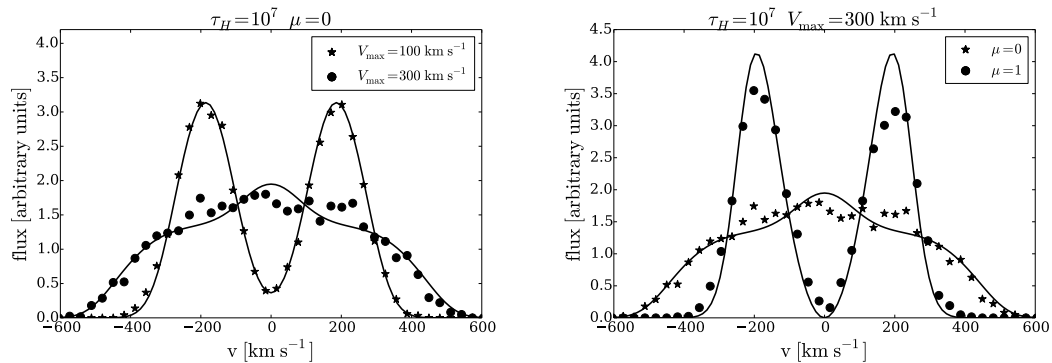
FIGURE 2.11: Comparison of the Monte Carlo results against the analytic solution. The left panel explores the results of different velocities. The right panel presents the results for two different observers: paralel and perpendicular to the rotational axis, $\mu = 1$ and $\mu = 0$ respectively.

Line Center. Our models have shown that rotation enhances the flux density at line center (see Fig. **2.4**). It has recently been proposed that galaxies with Lya spectral lines that contain flux at line center may be 'leaking' ionizing (LyC) photons [**34**?]. The main reason for this possible connection is that the escape of ionizing (LyC) photons requires $N_{HI} < 10^{17} \mathrm{cm}^{-2}$. The same low column densities facilitate the escape of Lyα photons at (or close to) line center. Our work suggests that rotation may provide an alternative explanation. **Single peaked lines.** The presence of single peaked profiles has been associated to inflow/outflow dynamics [**21**, **32**]. Gas bulk rotation can also be considered as a probable origin for that behaviour, provided that the observed single peak is highly symmetric. Similarly, in the case of double peaked lines with a high level of flux at the line center, rotation also deserves to be considered in the pool of possible bulk flows responsible for that feature, specially if the two peaks have similar intensities. **Systemic velocities.** There are observational measurements for the velocity shift between the Lyα and other emission lines. In our study we find that the position of the peak maxima can suddenly change with rotation and viewing angle. Namely the line can become single peaked for high rotational velocities and viewing angles perpendicular to the rotation axis. **Galaxy simulations with gas rotation.** [**30**] studied Lyα line emission in two high resolution simulations of individual galaxies. The main purpose of their study was to assess the impact of two different ISM prescriptions. However, each simulated galaxy had a disc structure with a clear rotation pattern in the ISM and inflowing gas from the circum-galactic region. The configuration had an axial symmetry and they reported a strong dependence of both the escape fraction and the total line intensity as a function of the θ angle. From our study, none of

these two quantities has a dependence either on the inclination angle or the rotational velocity. We suggest that he effect reported by [**30**] is consistent with being a consequence of the different hydrogen optical depth for different viewing angles and not as an effect of the bulk rotation. Zero impact on the Lyα escape fraction. Study of high redshift LAEs in numerical simulation often requires the estimation of the Lyα escape fraction in order to compare their results against observations [**23**? –**26**]. Most of these models estimate the escape fraction from the column density of dust and neutral Hydrogen. The results of our simulation indicate that the rotational velocity does not induce additional uncertainties in those estimates.

2.5   Conclusions

In this paper we quantified for the first time in the literature the effects of gas bulk rotation in the morphology of the Lyα emission line in star forming galaxies. Our results are based on the study of an homogeneous sphere of gas with solid body rotation. We explore a range of models by varying the rotational speed, hydrogen optical depth, dust optical depth and initial distribution of Lyα photons with respect to the gas density. As a cross-validation, we obtained our results from two independently developed Monte-Carlo radiative transfer codes. Two conclusions stand out from our study. First, rotation clearly impacts the Lyα line morphology; the width and the relative intensity of the center of the line and its peaks are affected. Second, rotation introduces an anisotropy for different viewing angles. For viewing angles close to the poles the line is double peaked and it makes a transition to a single peaked line for high rotational velocities and viewing angles along the equator. This trend is clearer for spheres with homogeneously distributed radiation sources than it is for central sources. Remarkably, we find three quantities that are invariant with respect to the viewing angle and the rotational velocity: the integrated flux, the escape fraction and the average number of scatterings. These results helped us to construct the outgoing spectra of a rotating sphere as a superposition of spectra coming from a static configuration. This description is useful to describe the main quantitative features of the Monte Carlo simulations. Quantitatively, the main results of our study are summarized as follows.

- In all of our models, rotation induces changes in the line morphology for different values of the angle between the rotation axis and the LoS,

θ. The changes are such that for a viewing angle perpendicular to the rotation axis, and high rotational velocities the line becomes single peaked.

- The line width increases with rotational velocity. For a viewing angle perpendicular to the rotation axis This change approximately follows the functional form $\mathrm{FWHM}^2 = \mathrm{FWHM}_0^2 + (V_{\max}/\lambda)^2$, where $\mathbf{FWHM_0}$ indicates the line width for the static case and λ is a constant. We have determined this constant to be $\lambda_{\mathrm{c}} = 0.83 \pm 0.06$ and $\lambda_{\mathrm{h}} = 0.82 \pm 0.05$ for the central and homogeneous source distributions, respectively.

- At fixed rotational velocity the line width decreases as $|\mu|$ increases, i.e. the smallest value of the line width is observed for a line of sight parallel to the ration axis.

- The single peaked line emerges at viewing angles $\mu \sim 1$ for when the rotational velocity is close to than half the $\mathbf{FWHM_0}$.

Comparing our results with recent observed LAEs we find that morphological features such as high central line flux, single peak profiles could be explained by gas bulk rotation present in these LAEs. The definitive and clear impact of rotation on the Lyα morphology suggests that this is an effect that should be taken into account at the moment of interpreting high resolution spectroscopic data. In particular it is relevant to consider the joint effect of rotation the and ubiquitous outflows (M.C. Remolina-Gutierrez et al., in prep.) because rotation can lead to enhanced escape of Lyα at line center, which has also been associated with escape of ionizing (LyC) photons [**34**?]

Acknowledgments

our code benefits from the work of the IPython and Matplotlib communities [? ?]. We thank the referee for the suggestions that allowed us to greatly improve and better frame the interpretation of our simulations.

.1 Analytic Expression for the Lyα Spectrum emerging from Rotating Cloud

Lyα scattering through an optically thick gas cloud that is undergoing solid-body rotation (i.e. in which the angular speed around the rotation axis is identical for each hydrogen atom) proceeds identical as in a static cloud. In order to compute the spectrum emerging from a rotating cloud, we sum the spectra emerging from all surface elements of the cloud, weighted by their intensity. We adopt the geometry shown in Fig A.1 to derive an analytic expression of this emerging spectrum, Note that this geometry differs from the scheme shown in Fig 1 in the main body of the paper. The sightline
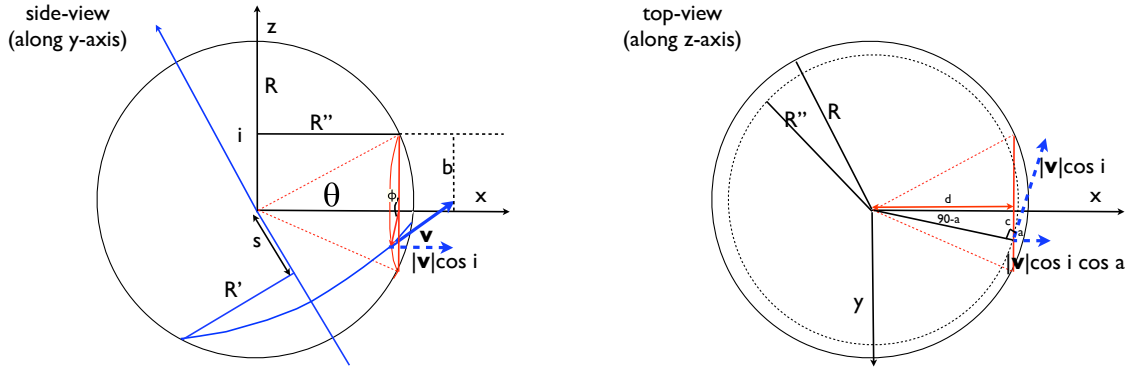
FIGURE 12: Adopted geometry for evaluating the analytic spectrum.

to the observer & rotation axis define the $x - z$ plane. The *left panel* in Fig A.1 shows the view from the y-axis. The observer sits along the x axis. The rotation axis makes an angle i with respect to the z-axis. We sum up spectra from individual patches by integrating over the impact parameter b, and angle ϕ. Each (b, ϕ) corresponds to a point on the sphere. This point has a velocity vector $\mathbf{v}(b, \phi, i)$, which we denote with $\mathbf{v}$ for brevity. The magnitude of $\mathbf{v}$ is $|\mathbf{v}| = V_{\max} R'/R$. Here $R' = \sqrt{R^2 - s^2}$, in which s denotes the distance of the point (b, ϕ) to the plane perpendicular to the rotation axis and through the origin (see the *left panel* of Fig A.1). This distance s is given by $s = |-\sin i \sqrt{R^2 - b^2} + b \cos \phi \cos i|$.

The spectrum of the flux emerging from the surface at point (b, ϕ) is

$$J(x, b, \phi, i) = \frac{\sqrt{\pi}}{\sqrt{24}a\tau_0} \left(\frac{(x - x_{\rm b})^2}{1 + \cosh\left[\sqrt{\frac{2\pi^3}{27}} \frac{|(x - x_{\rm b})^3|}{a\tau_0}\right]} \right),$$

where $x_b \equiv v_b/v_{\rm th}$, and v_b is the component of **v** projected onto the line-of-sight. This component is given by

$$v_{\rm b}(b, \phi, i) = V_{\max} \frac{\sqrt{R^2 - s^2}}{R} \cos i \, \cos a, \tag{6}$$

where $\beta = 90° - a$. The factor $\cos i$ accounts for the projection onto the $x - y$ plane, and the factor $\cos a$ for the subsequent projection onto the line-of-sight. The *right panel* of Fig. **A.1** shows that this angle a can be computed from

$$\tan \beta = \tan[90° - a] = \frac{c}{d} = \frac{b \sin \phi}{\sqrt{R^2 - b^2}}, \tag{7}$$

In order to compute to total intensity we integrate over b and ϕ with a weight given by the surface brightness of the sphere at (b, ϕ), $S(b, \phi)$.

$$J(x, i) = 2\pi \int_0^R db \, b \int_0^{2\pi} d\phi \, S(b, \phi) J(x, b, \phi, i) \approx 2\pi \int_0^R db \, b \int_0^{2\pi} d\phi \, J(x, b, \phi, i).$$

In the last expression we assume that $S(b, \phi)$ is constant. This corresponds to $I(\mu) \propto \mu$ at the surface, where μ denotes the cosine of the angle of the propagation direction of the outgoing photon and the normal to the spheres surface: a fixed db corresponds to a physical length $ds = db/\mu$ on the sphere. If $I(\mu)$ were constant, this would imply that the sphere should appear brighter per unit b. A constant surface brightness profile requires the directional dependence for $I(\mu) \propto \mu$ to correct for this. Indeed, this is what is expected for the escape of Lyα photons from static, extremely opaque media (see Ahn et al. [17]; their Fig 4 and accompanying discussion). It is worth stressing that this derivation should not be viewed as a complete analytic calculation, and we do not expect perfect agreement: we *assumed* a functional form for the surface brightness profile [or for $I(\mu)$]. Moreover, $I(\mu)$ itself may depend on frequency x. In other words, analytic solutions exist for $J(x) = \int_0^1 I(x, \mu) d\mu$ at the boundary of the sphere, and *approximate* expressions for $I(\mu) = \int dx I(x, \mu)$, but *not* for $I(x, \mu)$ itself. The spectra we obtained from the Monte-Carlo calculations naturally include the proper $I(x, \mu)$, and are therefore expected to be more accurate. To further test the assumption of scattering in a rotating medium proceeding as in a static medium we compute the distribution of the outgoing angles μ. The results are shown in Figure **A.2**; it shows that the

distribution for μ is independent of the rotational velocity and the location over the sphere. The only dependence comes with τ_H. For higher values of the optical depth the distribution gets closer to $I(\mu) \propto \mu$ as expected for a static medium [17].

FIGURE 13: Distribution of the cosine of the angle between the propagation direction and a vector normal to the sphere's surface. The distributions have been normalized to unity. Left panel: different rotational velocities; middle panel: different viewing angles; right panel: different optical depths. Only the optical depth has an effect on the distribution of outogoing directions. This is consistent with the assumption that Lyman α scattering in a medium with solid body rotation proceeds as in a static medium.

Appendix A

Analytic Expression for the Lyα Spectrum emerging from Rotating Cloud

Lyα scattering through an optically thick gas cloud that is undergoing solid-body rotation (i.e. in which the angular speed around the rotation axis is identical for each hydrogen atom) proceeds identical as in a static cloud. In order to compute the spectrum emerging from a rotating cloud, we sum the spectra emerging from all surface elements of the cloud, weighted by their intensity. We adopt the geometry shown in Fig **A.1** to derive an analytic expression of this emerging spectrum, Note that this geometry differs from the scheme shown in Fig 1 in the main body of the thesis. The sightline
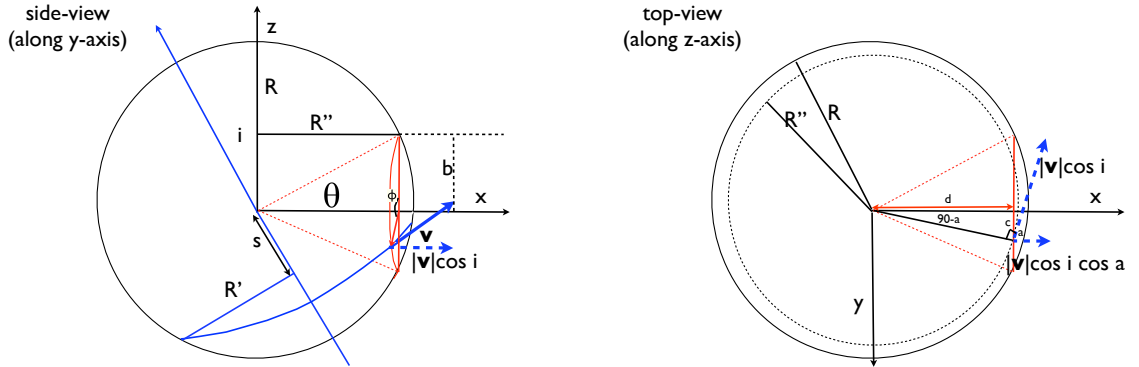

FIGURE A.1: Adopted geometry for evaluating the analytic spectrum.

to the observer & rotation axis define the $x - z$ plane. The *left panel* in Fig **A.1** shows the view from the y-axis. The observer sits along the x axis.

The rotation axis makes an angle i with respect to the z-axis. We sum up spectra from individual patches by integrating over the impact parameter b, and angle ϕ. Each (b, ϕ) corresponds to a point on the sphere. This point has a velocity vector $\mathbf{v}(b, \phi, i)$, which we denote with $\mathbf{v}$ for brevity. The magnitude of $\mathbf{v}$ is $|\mathbf{v}| = V_{\max} R'/R$. Here $R' = \sqrt{R^2 - s^2}$, in which s denotes the distance of the point (b, ϕ) to the plane perpendicular to the rotation axis and through the origin (see the *left panel* of Fig **A.1**). This distance s is given by $s = |-\sin i \sqrt{R^2 - b^2} + b \cos \phi \cos i|$.

The spectrum of the flux emerging from the surface at point (b, ϕ) is

$$J(x, b, \phi, i) = \frac{\sqrt{\pi}}{\sqrt{24} a \tau_0} \left(\frac{(x - x_{\mathrm{b}})^2}{1 + \cosh\left[\sqrt{\frac{2\pi^3}{27}} \frac{|(x - x_{\mathrm{b}})^3|}{a \tau_0} \right]} \right),$$

where $x_b \equiv v_b/v_{\mathrm{th}}$, and v_b is the component of $\mathbf{v}$ projected onto the line-of-sight. This component is given by

$$v_{\mathrm{b}}(b, \phi, i) = V_{\max} \frac{\sqrt{R^2 - s^2}}{R} \cos i \ \cos a, \tag{A.1}$$

where $\beta = 90° - a$. The factor $\cos i$ accounts for the projection onto the $x - y$ plane, and the factor $\cos a$ for the subsequent projection onto the line-of-sight. The *right panel* of Fig. **A.1** shows that this angle a can be computed from

$$\tan \beta = \tan[90° - a] = \frac{c}{d} = \frac{b \sin \phi}{\sqrt{R^2 - b^2}}, \tag{A.2}$$

In order to compute to total intensity we integrate over b and ϕ with a weight given by the surface brightness of the sphere at (b, ϕ), $S(b, \phi)$.

$$J(x, i) = 2\pi \int_0^R db \, b \int_0^{2\pi} d\phi \, S(b, \phi) J(x, b, \phi, i) \approx 2\pi \int_0^R db \, b \int_0^{2\pi} d\phi \, J(x, b, \phi, i).$$

In the last expression we assume that $S(b, \phi)$ is constant. This corresponds to $I(\mu) \propto \mu$ at the surface, where μ denotes the cosine of the angle of the propagation direction of the outgoing photon and the normal to the spheres surface: a fixed db corresponds to a physical length $ds = db/\mu$ on the sphere. If $I(\mu)$ were constant, this would imply that the sphere should appear brighter per unit b. A constant surface brightness profile requires the directional dependence for $I(\mu) \propto \mu$ to correct for this. Indeed, this is what is expected for the escape of Lyα photons from static, extremely opaque media (see Ahn et al. [17]; their Fig 4 and accompanying discussion). It is worth stressing that this derivation should not be viewed as a complete analytic calculation, and we do not expect perfect agreement: we *assumed* a functional form for the

surface brightness profile [or for $I(\mu)$]. Moreover, $I(\mu)$ itself may depend on frequency x. In other words, analytic solutions exist for $J(x) = \int_0^1 I(x,\mu)d\mu$ at the boundary of the sphere, and *approximate* expressions for $I(\mu) = \int dx I(x,\mu)$, but *not* for $I(x,\mu)$ itself. The spectra we obtained from the Monte-Carlo calculations naturally include the proper $I(x,\mu)$, and are therefore expected to be more accurate. To further test the assumption of scattering in a rotating medium proceeding as in a static medium we compute the distribution of the outgoing angles μ. The results are shown in Figure **A.2**; it shows that the distribution for μ is independent of the rotational velocity and the location over the sphere. The only dependence comes with τ_H. For higher values of the optical depth the distribution gets closer to $I(\mu) \propto \mu$ as expected for a static medium [**17**].

FIGURE A.2: Distribution of the cosine of the angle between the propagation direction and a vector normal to the sphere's surface. The distributions have been normalized to unity. Left panel: different rotational velocities; middle panel: different viewing angles; right panel: different optical depths. Only the optical depth has an effect on the distribution of outgoing directions. This is consistent with the assumption that Lyman α scattering in a medium with solid body rotation proceeds as in a static medium.

Bibliography

[1] R. B. Partridge and P. J. E. Peebles. Are Young Galaxies Visible? *ApJ*,147:868, March 1967. doi: 10.1086/149079.

[2] J. E. Rhoads, S. Malhotra, A. Dey, D. Stern, H. Spinrad, and B. T. Jannuzi. First Results from the Large-Area Lyman Alpha Survey. *ApJ*,545: L85–L88, December 2000. doi: 10.1086/317874.

[3] E. Gawiser, H. Francke, K. Lai, K. Schawinski, C. Gronwall, R. Ciardullo, R. Quadri, A. Orsi, L. F. Barrientos, G. A. Blanc, G. Fazio, and J. J. Feldmeier. Lyα-Emitting Galaxies at z = 3.1: L* Progenitors Experiencing Rapid Star Formation. *ApJ*, 671:278–284, December 2007. doi: 10.1086/522955.

[4] R. S. Koehler, P. Schuecker, and K. Gebhardt. Probing dark energy with baryonic acoustic oscillations at high redshifts. *aap*, 462:7–20, January 2007. doi: 10.1051/0004-6361:20065649.

[5] M. Ouchi, K. Shimasaku, M. Akiyama, C. Simpson, T. Saito, Y. Ueda, H. Furusawa, K. Sekiguchi, T. Yamada, T. Kodama, N. Kashikawa, S. Okamura, M. Iye, T. Takata, M. Yoshida, and M. Yoshida. The Subaru/XMM-Newton Deep Survey (SXDS). IV. Evolution of Lyα Emitters from z=3.1 to 5.7 in the 1 deg^2 Field: Luminosity Functions and AGN. *ApJs*, 176:301–330, June 2008. doi: 10.1086/527673.

[6] T. Yamada, Y. Nakamura, Y. Matsuda, T. Hayashino, R. Yamauchi, N. Morimoto, K. Kousai, and M. Umemura. Panoramic Survey of Lyα Emitters at z = 3.1. *Aj*, 143:79, April 2012. doi: 10.1088/0004-6256/ 143/4/79.

[7] M. A. Schenker, D. P. Stark, R. S. Ellis, B. E. Robertson, J. S. Dunlop, R. J. McLure, J.-P. Kneib, and J. Richard. Keck Spectroscopy of Faint 3 z 8 Lyman Break Galaxies: Evidence for a Declining Fraction of

Emission Line Sources in the Redshift Range 6 z 8. *ApJ*, 744:179, January 2012. doi: 10.1088/0004-637X/744/2/179.

[8] S. L. Finkelstein, C. Papovich, M. Dickinson, M. Song, V. Tilvi, a. M. Koekemoer, K. D. Finkelstein, B. Mobasher, H. C. Ferguson, M. Giavalisco, N. Reddy, M. L. N. Ashby, a. Dekel, G. G. Fazio, a. Fontana, N. a. Grogin, J.-S. Huang, D. Kocevski, M. Rafelski, B. J. Weiner, and S. P. Willner. A galaxy rapidly forming stars 700 million years after the Big Bang at redshift 7.51. *Nature*, 502(7472):524–527, October 2013. ISSN 0028-0836. doi: 10.1038/nature12657. URL http://www.nature.com/doifinder/10.1038/nature12657.

[9] T. F. Adams. The Escape of Resonance-Line Radiation from Extremely Opaque Media. *ApJ*, 174:439, June 1972. doi: 10.1086/151503.

[10] J. P. Harrington. The scattering of resonance-line radiation in the limit of large optical depth. *MNRAS*, 162:43, 1973.

[11] D. A. Neufeld. The transfer of resonance-line radiation in static astrophysical media. *ApJ*, 350:216–241, February 1990. doi: 10.1086/168375.

[12] M. Dijkstra, Z. Haiman, and M. Spaans. Lyα Radiation from Collapsing Protogalaxies. I. Characteristics of the Emergent Spectrum. *ApJ*, 649: 14–36, September 2006. doi: 10.1086/506243.

[13] A. Loeb and G. B. Rybicki. Scattered Lyα Radiation around Sources before Cosmological Reionization. *ApJ*, 524:527–535, October 1999. doi: 10.1086/307844.

[14] L. H. Auer. Transfer of Lyman Alpha in Diffuse Nebulae. *ApJ*, 153:783, September 1968. doi: 10.1086/149705.

[15] L. W. Avery and L. L. House. An Investigation of Resonance-Line Scattering by the Monte Carlo Technique. *ApJ*, 152:493, May 1968. doi: 10.1086/149566.

[16] S.-H. Ahn, H.-W. Lee, and H. M. Lee. Ly Alpha Transfer in a Thick, Dusty, and Static Medium. *Journal of Korean Astronomical Society*, 33:29–36, April 2000.

[17] S.-H. Ahn, H.-W. Lee, and H. M. Lee. Lyα Line Formation in Starbursting Galaxies. I. Moderately Thick, Dustless, and Static H I Media. *ApJ*, 554:604–614, June 2001. doi: 10.1086/321374.

[18] Z. Zheng and J. Miralda-Escudé. Monte Carlo Simulation of Lyα Scattering and Application to Damped Lyα Systems. *ApJ*, 578:33–42, October 2002. doi: 10.1086/342400.

[19] M. Hansen and S. P. Oh. Lyman α radiative transfer in a multiphase medium. *MNRAS*, 367:979–1002, April 2006. doi: 10.1111/j.1365-2966. 2005.09870.x.

[20] S.-H. Ahn, H.-W. Lee, and H. M. Lee. P Cygni type Lyα from starburst galaxies. *MNRAS*, 340:863–869, April 2003. doi: 10.1046/j.1365-8711. 2003.06353.x.

[21] A. Verhamme, D. Schaerer, and A. Maselli. 3D Lyα radiation transfer. I. Understanding Lyα line profile morphologies. *AAP*, 460:397–413, December 2006. doi: 10.1051/0004-6361:20065554.

[22] M. Dijkstra. Lyman Alpha Emitting Galaxies as a Probe of Reionization. *ArXiv e-prints, arXiv:1406.7292*, June 2014.

[23] A. Orsi, C. G. Lacey, and C. M. Baugh. Can galactic outflows explain the properties of Ly α emitters? *MNRAS*, 425:87–115, September 2012. doi: 10.1111/j.1365-2966.2012.21396.x.

[24] T. Garel, J. Blaizot, B. Guiderdoni, D. Schaerer, A. Verhamme, and M. Hayes. Modelling high redshift Lyman α emitters. *MNRAS*, 422: 310–325, May 2012. doi: 10.1111/j.1365-2966.2012.20607.x.

[25] J. E. Forero-Romero, G. Yepes, S. Gottlöber, S. R. Knollmann, A. J. Cuesta, and F. Prada. CLARA's view on the escape fraction of Lyman α photons in high-redshift galaxies. *MNRAS*, 415:3666–3680, August 2011. doi: 10.1111/j.1365-2966.2011.18983.x.

[26] J. E. Forero-Romero, G. Yepes, S. Gottlöber, and F. Prada. Modelling the fraction of Lyman break galaxies with strong Lyman α emission at 5 ≤ z ≤ 7. *MNRAS*, 419:952–958, January 2012. doi: 10.1111/j.1365-2966. 2011.19744.x.

[27] C. Behrens and J. Niemeyer. Effects of Lyman-alpha scattering in the IGM on clustering statistics of Lyman-alpha emitters. *AAP*, 556:A5, August 2013. doi: 10.1051/0004-6361/201321172.

[28] P. Laursen, J. Sommer-Larsen, and A. C. Andersen. Lyα Radiative Transfer with Dust: Escape Fractions from Simulated High-Redshift

Galaxies. *ApJ*, 704:1640–1656, October 2009. doi: 10.1088/0004-637X/704/2/1640.

[29] L. A. Barnes, M. G. Haehnelt, E. Tescari, and M. Viel. Galactic winds and extended Lyα emission from the host galaxies of high column density quasi-stellar object absorption systems. *MNRAS*, 416:1723–1738, September 2011. doi: 10.1111/j.1365-2966.2011.18789.x.

[30] A. Verhamme, Y. Dubois, J. Blaizot, T. Garel, R. Bacon, J. Devriendt, B. Guiderdoni, and A. Slyz. Lyman-α emission properties of simulated galaxies: interstellar medium structure and inclination effects. *AAP*, 546:A111, October 2012. doi: 10.1051/0004-6361/201218783.

[31] H. Yajima, Y. Li, Q. Zhu, T. Abel, C. Gronwall, and R. Ciardullo. Were Progenitors of Local L* Galaxies Lyα Emitters at High Redshift? *ApJ*, 754:118, August 2012. doi: 10.1088/0004-637X/754/2/118.

[32] M. Dijkstra and R. Kramer. Line transfer through clumpy, large-scale outflows: Ly α absorption and haloes around star-forming galaxies. *MNRAS*, 424:1672–1693, August 2012. doi: 10.1111/j.1365-2966.2012.21131.x.

[33] Z. Zheng and J. Wallace. Anisotropic Lyman-alpha Emission. *ArXiv e-prints*, August 2013.

[34] C. Behrens, M. Dijkstra, and J. C. Niemeyer. Beamed Lyα emission through outflow-driven cavities. *AAP*, 563:A77, March 2014. doi: 10.1051/0004-6361/201322949.